Highly selective oxidation of methane to acetic acid enabled by deficient UiO-66 under mild conditions

Yaowen Wei [a], Jianwei Wang [a], Hao Guo [a,*], Tao Ban[a], Yufeng Yue [a], Di Hu [a,*], Haibao Huang [a,b,*]

[a] Xinjiang Key Laboratory of Coal Clean Conversion & Chemical Engineering Process, School of Chemical Engineering and Technology, Xinjiang University, Urumqi 830046, Xinjiang, China.

[b] School of Environmental Science and Engineering, Sun Yat-sen University, Guangzhou 510275, China

* Corresponding author E-mail addresses: guohao@xju.edu.cn (Hao Guo), hudi13@126.com (Di Hu), seabao8@gmail.com (Haibao Huang).

KEYWORDS: Methane; Selective oxidation; Acetic acid; UiO-66; Defect engineering

Catalyst characterization

The X-ray diffraction (XRD) test was recorded using Cu Kα (λ = 1.54056 Å) radiation on the Rigaku Ultima IV X-ray instrument. The X-ray diffraction wavelength was 1.54056 Å, the beam voltage was 40 kV, the current was 40 mA, and the scanning speed was 2 ° / min.

The N_2 adsorption and desorption isotherms were obtained by ASAP 2020 automatic volume adsorption analyzer. Before the test, the samples were vacuum activated at 150 ℃ for 4 h, and then the nitrogen adsorption-desorption isotherms were measured at -200 °C. The specific surface area was calculated by BET formula.

The high resolution field emission scanning electron microscope / energy spectrum analyzer (STEM) test was performed using the SU8220 of Hitachi, Japan, with an acceleration voltage of 0.5 kV-30 kV, and the morphology of the sample was observed. The high-resolution transmission electron microscope / energy spectrum analyzer (TEM) is based on the JEOL JEM-2100 F of Japan Co., Ltd. The operating voltage is 200 kV, the point resolution is 0.23 nm, the line resolution is 0.10 nm, and the STEM probe and the Oxford company's electric refrigeration energy spectrometer system X-Max80 T are included.

XPS characterization was performed using an Axis Ultra DLD photoelectron spectrometer produced by Kratos. The test conditions: monochromatic Al Kα (hν = 1486.6 eV) as the radiation source, a concentric spherical analyzer for parallel imaging, and a C1 s peak at 284.6 eV to calibrate all spectral binding energies.

Fourier transform infrared spectroscopy (FTIR) characterization can be used to analyze the functional groups in the sample. FTIR characterization was performed using a BRUKER TENSOR 27 infrared spectrometer. During the test, 1-2 mg of the sample was mixed with 200 mg of pure KBr and ground evenly. The ground powder was placed in a mold and pressed into transparent sheets with a pressure of 5 MPa on an oil press for testing. Both the sample and KBr need to be dried and ground to a particle size of less than 2 μm to avoid the influence of scattered light.

UV-visible absorption spectra were recorded by UV-2600i scanning spectrophotometer (Shimadzu).

Electron paramagnetic resonance (EPR) spectroscopy was recorded on a Bruker A300 spectrophotometer equipped with a liquid nitrogen cryostat. 5,5-Dimethyl-1-pyrroline-N-oxide (DMPO) was used as a free radical scavenger to detect the types of free radicals produced by the interaction of CH_4 with H_2O_2. Free radicals are represented by species prefixed with the symbol '·'. For example, the hydroxyl and methyl radicals are represented by '·OH' and '·CH_3', respectively.

In-situ diffuse reflectance infrared Fourier transform (in-situ DRIFTS) spectroscopy was performed on a Thermo-Fisher Nicolet iS20 instrument equipped with a liquid nitrogen-cooled mercury cadmium tellurium (MCT) detector. All samples were pretreated with 20 mL / min N_2 at 120 °C to remove water and impurities adsorbed on the catalyst surface, and then the background spectra were collected. After adjusting the reaction temperature to the reaction temperature, the airflow containing CH_4 and H_2O_2 was swept for 120 minutes, and 64 scans were collected at a resolution of 4 cm^{-1} in the wavelength range of 4000-650 cm^{-1}.

Setting the TFA dosage gradient in the UiO-66-XT catalyst

TFA was added for tempering treatment during the synthesis of UiO-66. During the defect generation phase, TFA was added at concentrations of 0.1, 0.3 and 0.35 ml. This gradient design aimed to cover three representative regions -the 'minimum zone', 'optimal zone' and 'excess zone' - to systematically establish the relationship between defect levels and catalytic performance. A more comprehensive ratio configuration is detailed in the Supporting Materials section.

Computational methodology

This study uses the Vienna Ab initio Simulation Package (VASP, version 5.4.1) within the density functional theory (DFT) computational framework. The projected augmented wave (PAW) method is used to describe the potential function and the exchange-correlation interaction between electrons is handled using the Perdew-Burke-Ernzerhof (PBE) functional within the generalized gradient approximation (GGA). Setting the energy cutoff of the plane-wave basis set to 400 eV achieves computational results comparable to those obtained with higher cutoffs, while offering greater computational efficiency. Therefore, this value was selected as the plane-wave energy cutoff for the present calculations. To prevent interlayer interactions arising from periodic boundary conditions, a 15 Å vacuum layer was introduced along the z-direction. The energy convergence criterion for structural optimization was set to 10^{-5} eV and the residual force convergence criterion to 0.02 eV/Å.

Quantitative analysis methods for the numbers of ligand-vacancies

The numbers of ligand-vacancies coordinated per metal node were calculated by TG analysis using a method proposed by Shearer et al [1].

The ideal combustion of one-unit UiO-66 under TG analysis (air) produces 6 units of ZrO_2 as the residual.

$$Zr_6O_6(BDC)_6 + 45\ O_2 \longrightarrow 6ZrO_2 + 48\ CO_2 + 12H_2O$$

The ideal formula of a UiO-66 MOF is ($Zr_6O_6(BDC)_6$, MW = 1628.03, which is 2.202 times higher than the MW of $6ZrO_2$. Hence, the ideal TG plateau should be at 220.2% ($W_{Idea\ Plat}$) when the end weight of TG analysis was normalized to 100%, attributed to the ZrO_2 (W_{ZrO2}). However, in real practice, there is always a deviation that occurs from the ideal plateau resulting from the defect induced in the framework. The extent of the defect can be calculated based on the number of linkers absent per metal node. The general formula of defective UiO-66 based on the number of ZrO_2 H_2BDC linkers would be $Zr_6O_{6+x}(BDC)_{6-x}$

6+x = indicates the charge balance due to the ligand-vacancies in the framework is compensated by the extra oxide anion

6-x = number of linkers per Zr_6 node

x = number of linkers absent per Zr_6 node

The ideal weight contribution per H_2BDC linker can be obtained by,

$$\frac{W_{Idea\ Plat}-W_{ZrO2}}{6} = \frac{220.2\%-100\%}{6} = 20.03\% \quad (1)$$

Now considering the general formula for defective UiO-66, the actual number of H_2BDC linkers per Zr_6 node can be obtained by,

$$\frac{\text{Experimental TGA plateau}-W_{ZrO2}}{20.03\%} \quad (2)$$

On putting the value of the experimental TGA plateau ($W_{Exp.\ plat}$) obtained from TG analysis in Fig. 3a-d, the actual number of H_2BDC linkers connected per node can be calculated.

For UiO-66-0.1T, $(6\text{-}x) = \frac{180.2\%-100\%}{20.03\%} = 4.0$.

Since the absence of ligands could create two ligand-vacancies, the numbers of ligand-vacancies per Zr_6 node are (6-x)*2 = (6-4)*2 = 4.

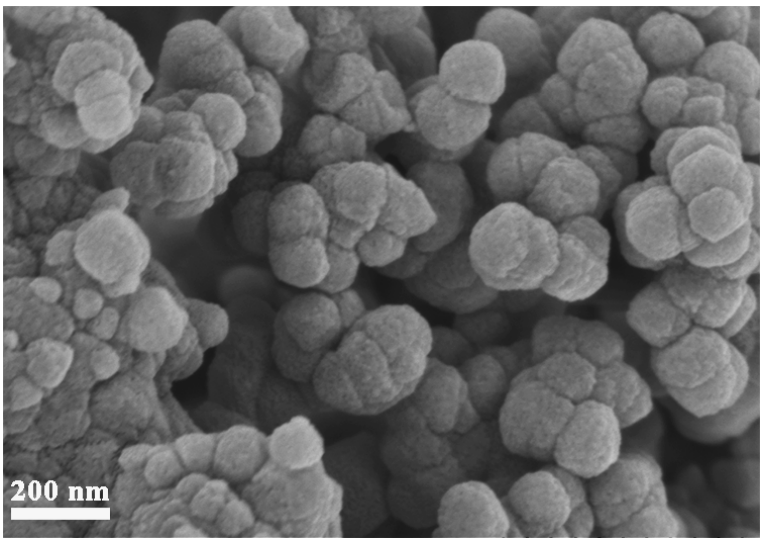

Fig. S1 SEM image of UiO-66.

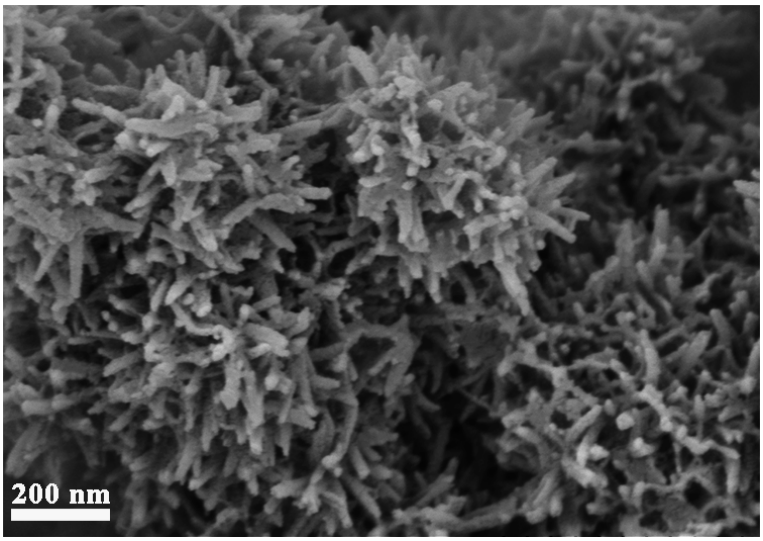

Fig. S2 SEM image of UiO-66-0.3T.

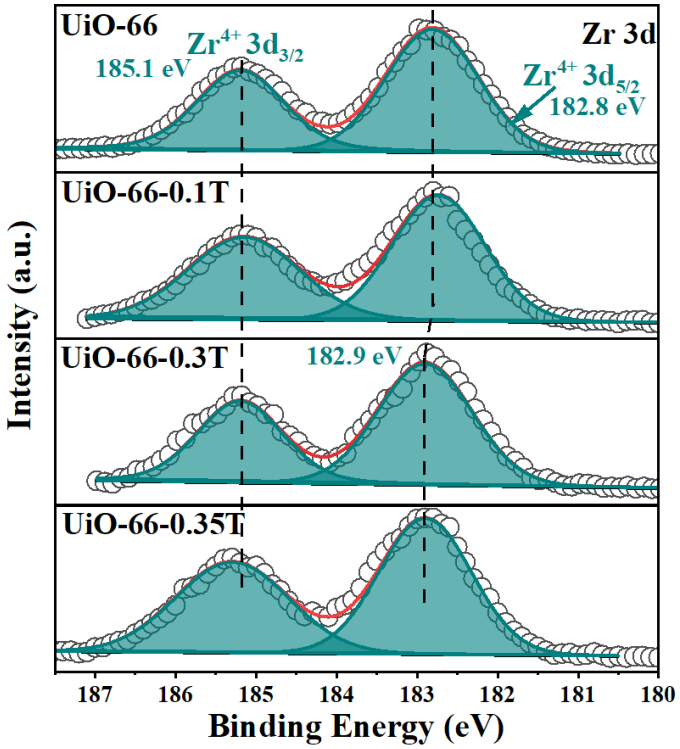

Fig. S3 XPS spectra of UiO-66 and UiO-66-XT: Zr 3*d*.

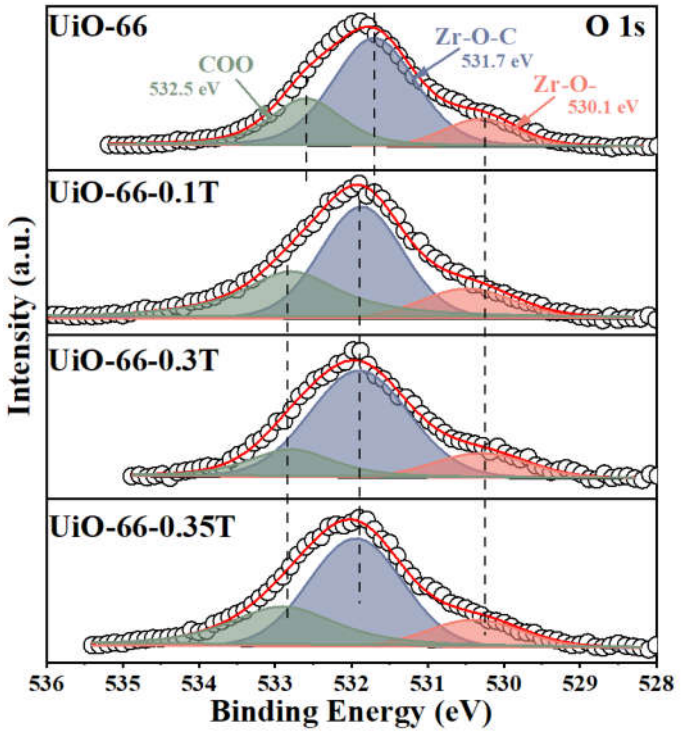

Fig. S4 XPS spectra of UiO-66 and UiO-66-XT: O 1*s*.

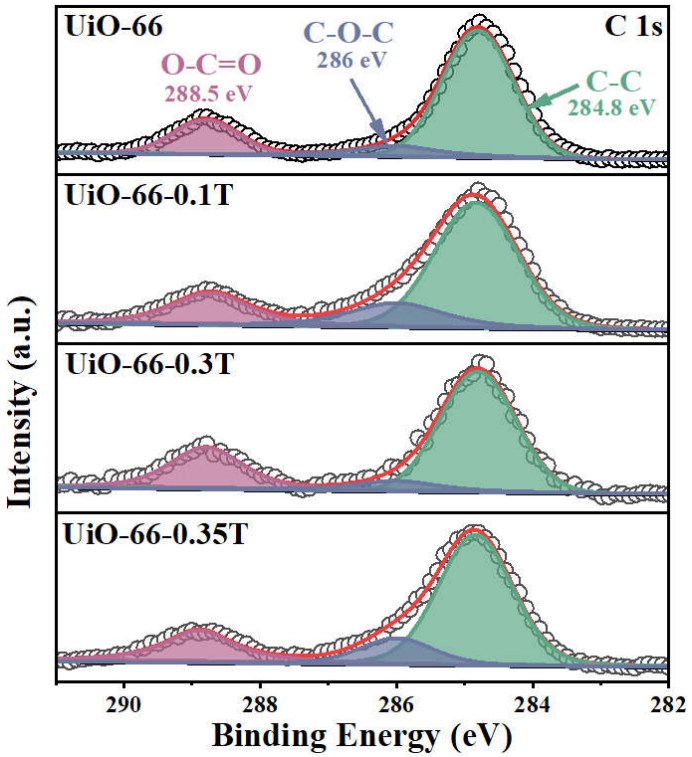

Fig. S5 XPS spectra of UiO-66 and UiO-66-XT: C 1*s*.

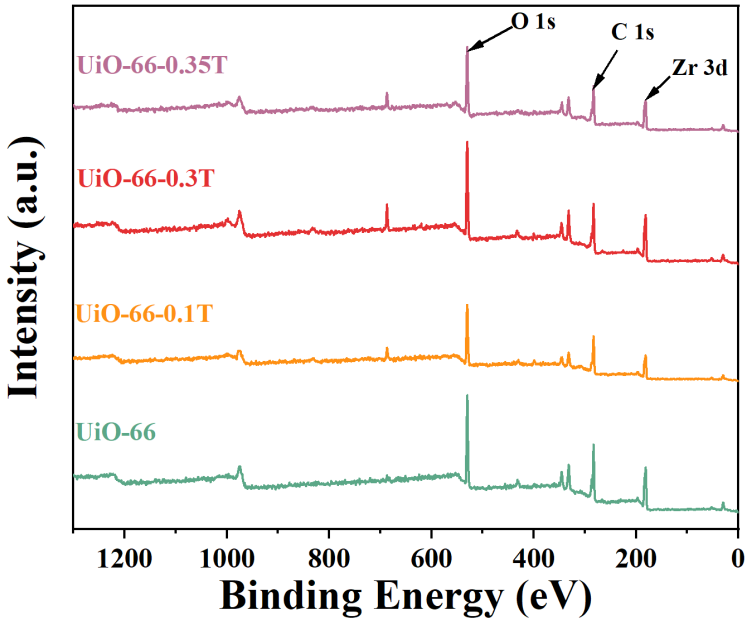

Fig. S6 XPS spectra of Full spectrum.

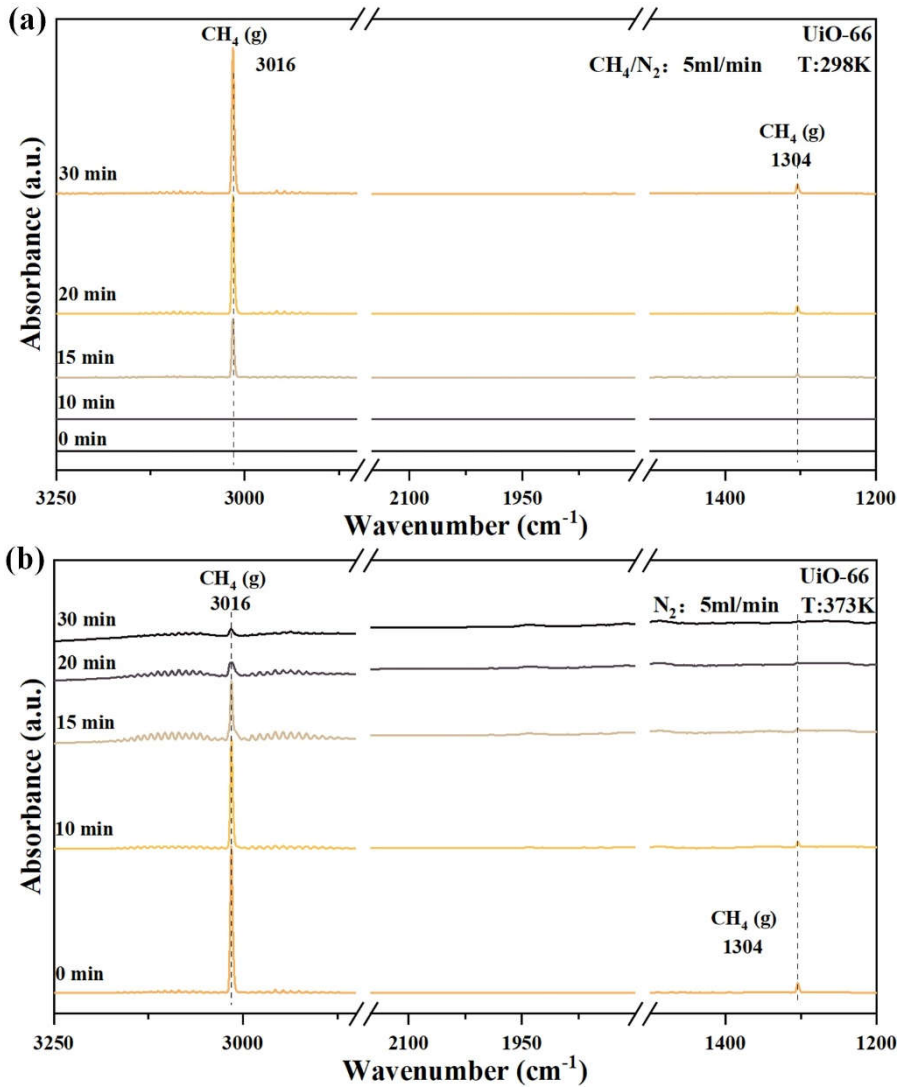

Fig. S7 (a) Adsorption of CH_4 by UiO-66 at 298K. (b) Desorption of CH_4 at UiO-66 by N_2 flowing at 373K.

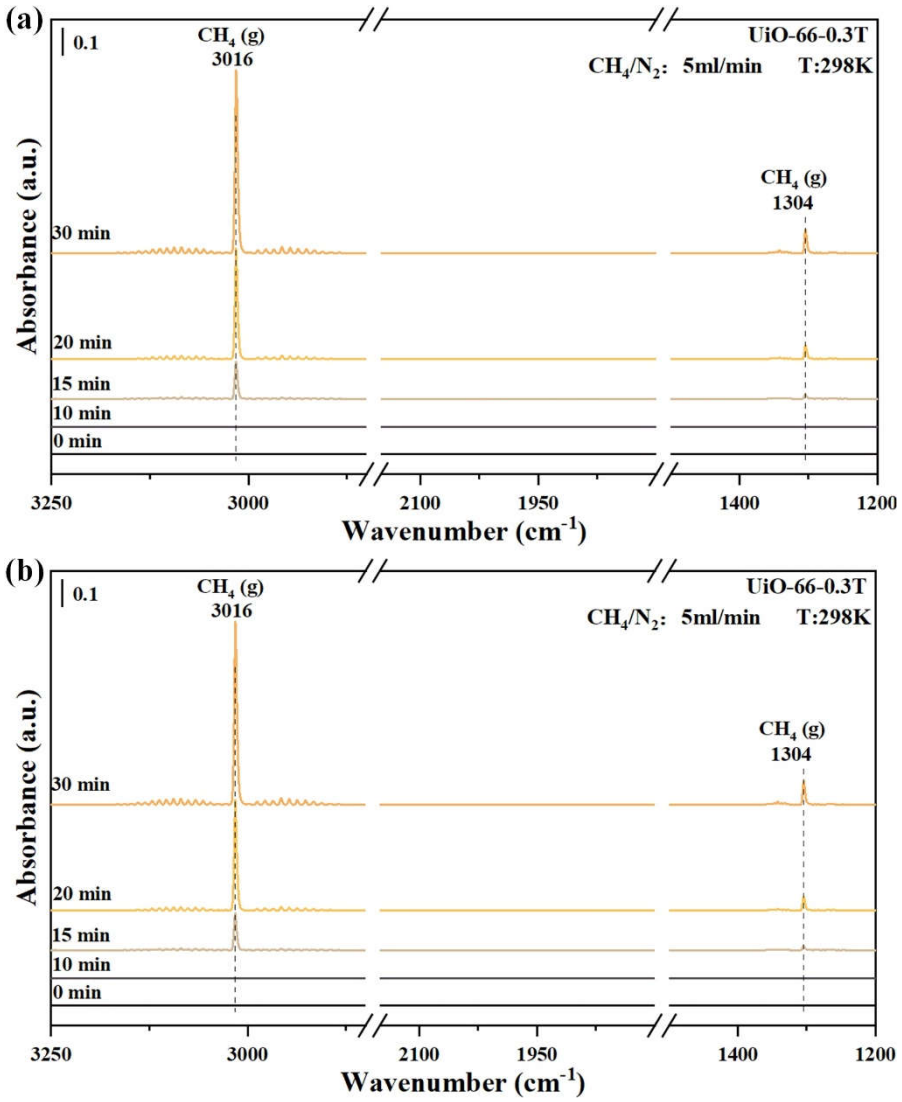

Fig. S8 (a) Adsorption of CH_4 by UiO-66-0.3T at 298K. (b) Desorption of CH_4 at UiO-66-0.3T by N_2 flowing at 373K.

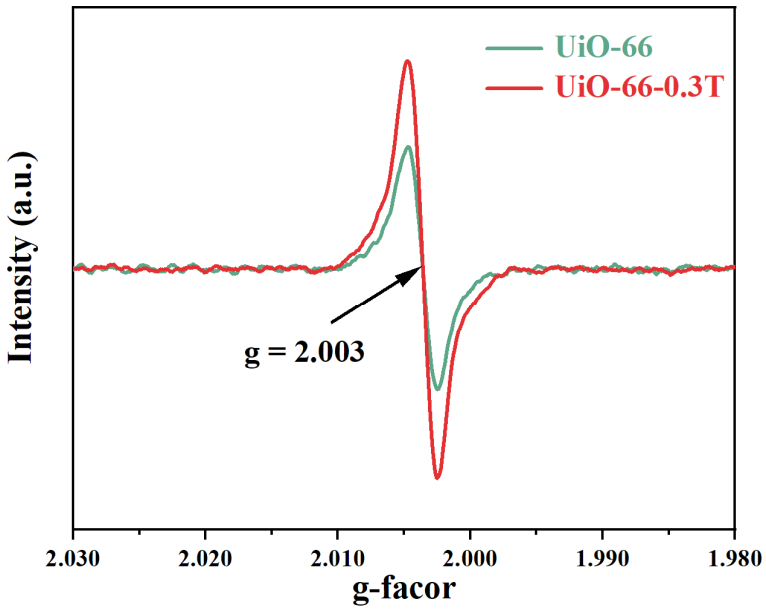

Fig. S9 The EPR spectra of UiO-66 and UiO-66-0.3T.

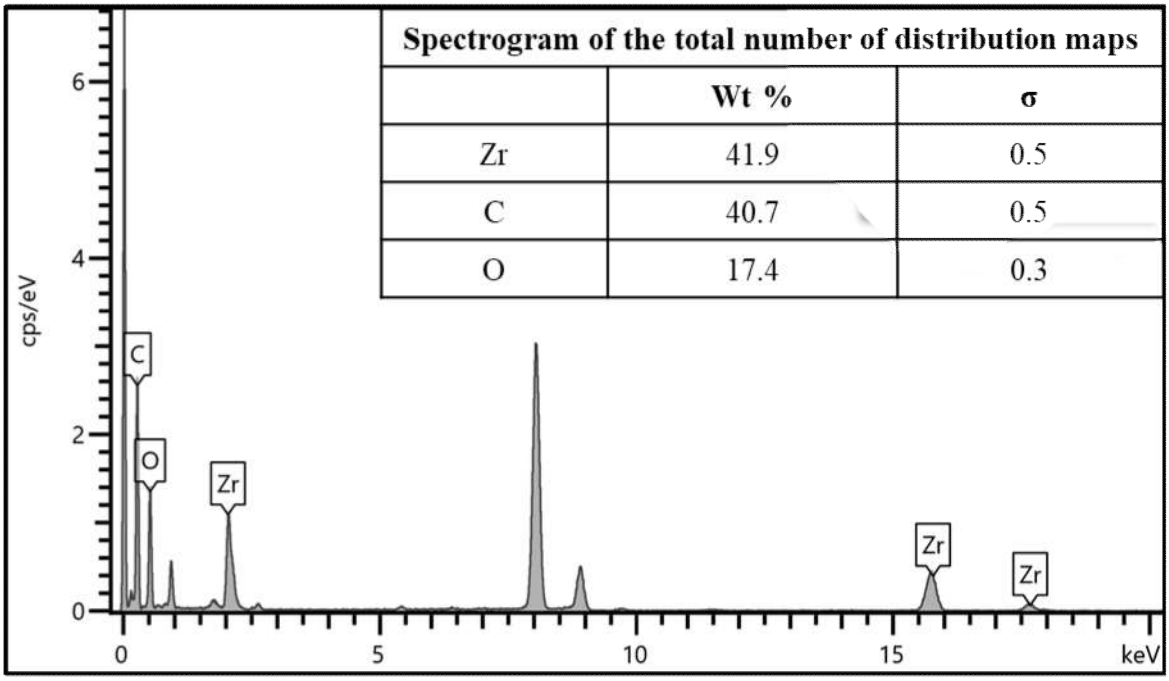

Fig. S10 The Spectrogram of the total number of distribution maps.

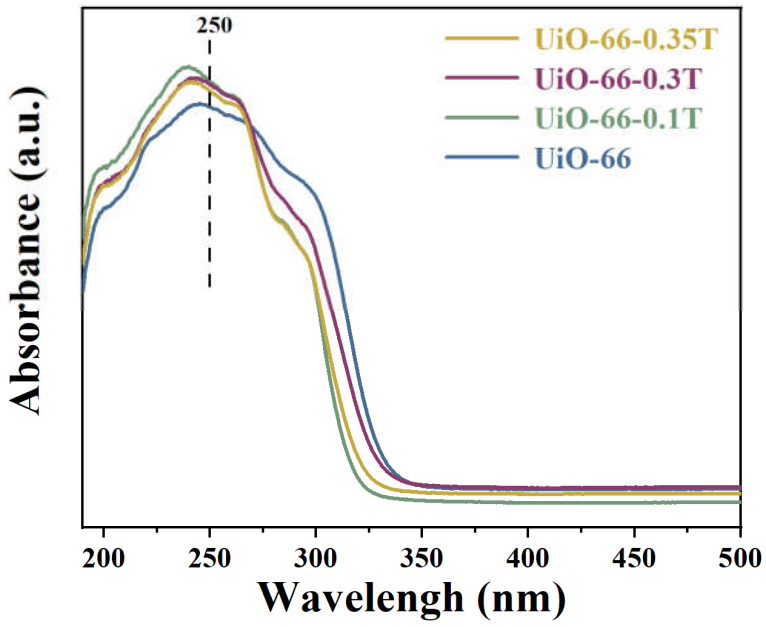

Fig. S11 The UV-vis spectra of UiO-66 and UiO-66-0.3T.

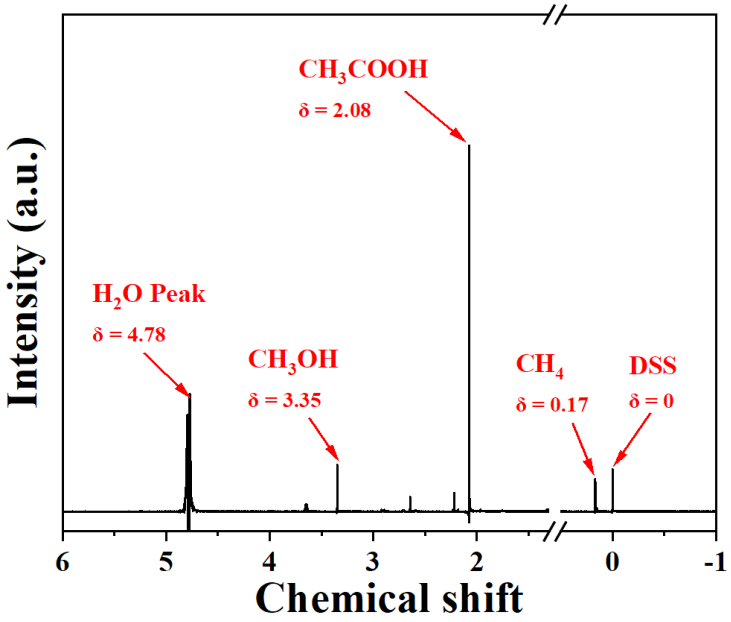

Fig. S12 ^{1}H NMR spectra of Oxygenated compounds.

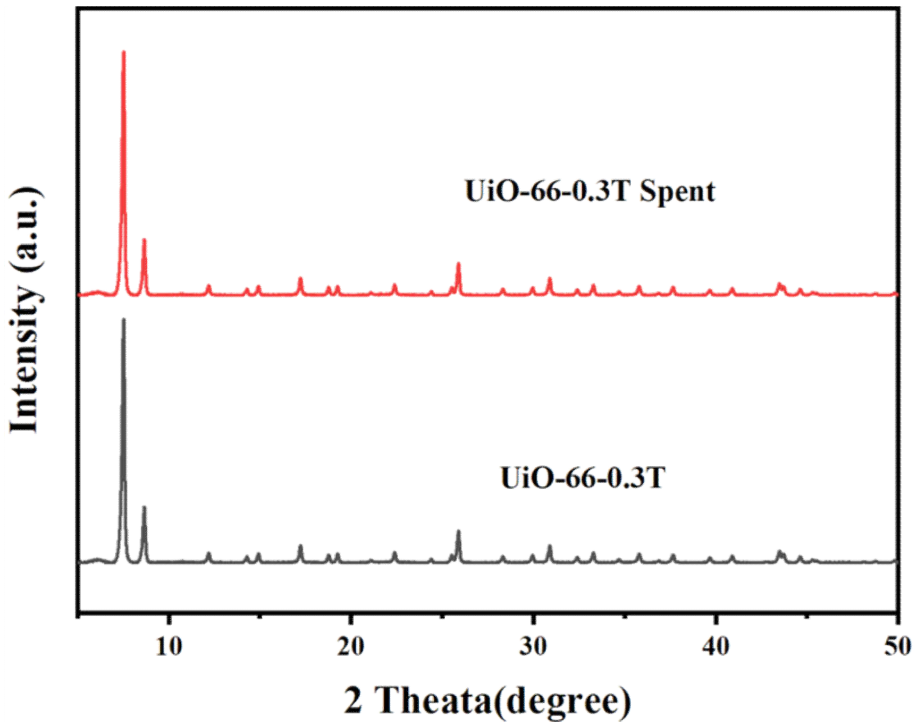

Fig. S13 XRD patterns of UiO-66-0.3T catalysts before and after 3 cycle test.

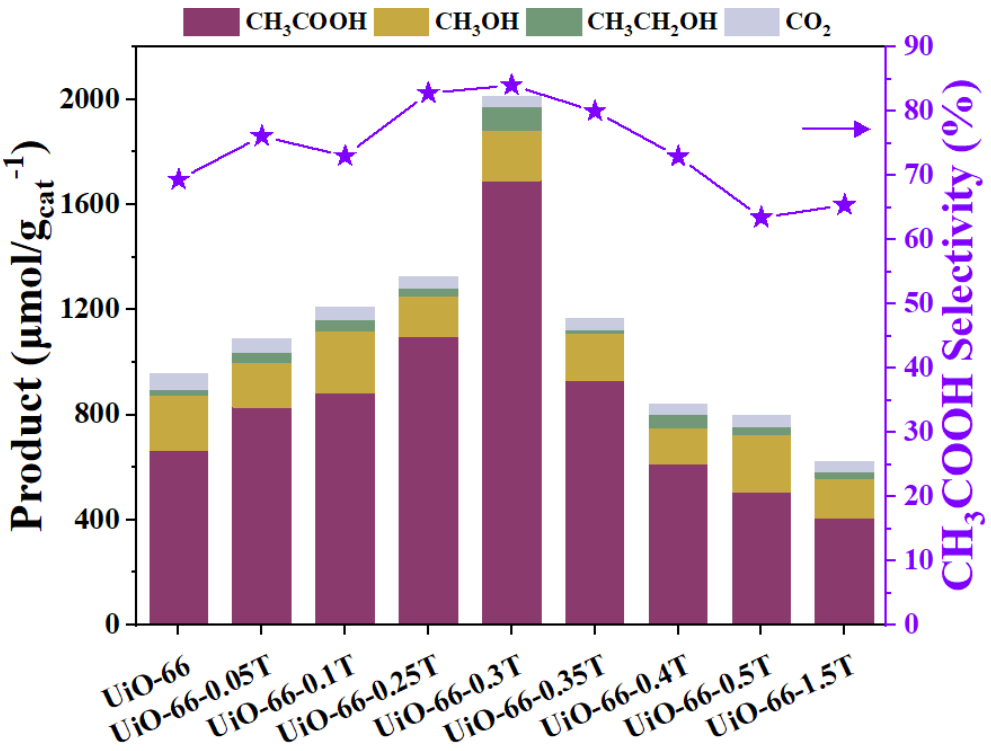

Fig. S14 The catalytic performance of UiO-66-XT modulated by TFA with different addition amount. Reaction condition: 10 mL 5% H_2O_2, 30 bar CH_4, catalyst amount: 30 mg, reaction temperature: 150 ℃, reaction time: 6 h.

Table S1. Physicochemical properties for UiO-66-XT.

Catalyst	A_{BET}[a] ($m^2 \cdot g^{-1}$)	A_{micro}[b] ($m^2 \cdot g^{-1}$)	V_{micro}[b] ($cm^3 \cdot g^{-1}$)	R_{BJH}[c] (nm)
UiO-66	650.8	650.8	0.22	0.43
UiO-66-0.1T	954.9	954.9	0.36	0.46
UiO-66-0.3T	1043.3	1043.3	0.39	0.47
UiO-66-0.35T	984.4	984.4	0.36	0.48

[a] Detected by BET analysis.

[b] Collected after the t-plot run.

[c] The average pore radius of BJH adsorption.

Table S2. Acetic acid formation rate in 6 h upon UiO-66 under different experimental conditions.

Experimental conditions	**Acetic acid yield / µmol $g_{cat.}^{-1}$**
No Catalyst	Not detected
No Methane	Not detected
No H_2O_2	Not detected
UiO-66-0.3T+Methane+H_2O_2	1691

Table S3. The third cycle test of the UiO-66-0.3T catalyst involved the measurement of the Zr^{4+} content in liquid products.

Number of cycles	Zr^{4+} content in liquid products (%) [a]
RUN 1	0.000021
RUN 2	0.000016
RUN 3	0.000024

[a]ICP-OES determination of Zr^{4+} content in liquid products.

Table S4. Comparison of the TOF and selectivity of acetic acid under different systems.

	Catalyst + promoter	Reaction temperature / ℃	Reaction time / h	Reactant + additive	Acetic acid yield / μmol $g_{cat.}^{-1}$	Acetic acid selectivity in all oxygenates / %	Ref.
1	UiO-66-0.3T	150	6	3 MPa CH_4 / 10 ml 5% H_2O_2	1691	84	This work
2	Rh_1-Cu/POPs	150	2	3 MPa CH_4 / 1 MPa CO / 0.5 MPa O_2 / 20 mL H_2O / C_6H_5I	860	6.9	[2]
3	UiO-67-Pt-Z	60	4	5 MPa CH_4 / 5 mL 30% H_2O_2	121.3	21.9	[3]
4	Vanadium-based MOFs (MOF-48/ MIL47)	80	20	4 mmol $K_2S_2O_8$ / 7.5 mL CF_3COOH / 1 MPa CH_4	490	91	[4]
				4 mmol $K_2S_2O_8$ / 7.5 mL CF_3COOH / 1 MPa CH_4 / 1 MPa CO	686	100	
5	Fe-BN/ZSM-5	30	6	20 mL H_2O / 0.5 MPa 97% CO/N_2 / 2.5 MPa 95% CH_4/Ar / 654 mmol H_2O_2	610	66	[5]
6	1.2Ni-ZSM-5	50	10	0.5MPa CO / 2.5 MPa CH_4 / 654μmol H_2O_2 / 20ml H_2O	2920	82	[6]
7	Au-ZSM-5	240	1	2 MPa CH_4 / 0.5 MPa CO / 0.4 MPa O_2 / 20 mL H_2O	20	12.4	[7]

Table S5. ^{1}H NMR chemical shift of various compounds.

Compounds	Formula	Chemical shift (multiplicity)
Methane	CH_4	δ, 0.17 ppm, s
Acetic Acid	CH_3COOH	δ, 2.07 ppm, s
Methanol	CH_3OH	δ, 3.35 ppm, s
Methyl Hydroperoxide	CH_3OOH	δ, 3.85 ppm, s
Water	H_2O	δ, 4.75 ppm, s
Formic Acid	$HCOOH$	δ, 8.24 ppm, s

References

[1] S. C. Shearer, S. Chavan, S. Bordiga, S. Svelle, U. Olsbye, K. P. Lillerud, *Chem. Mater.*, **2016**, 28, 3749–3761.

[2] B. Li, X. G Song, S. Q. Feng, Q. Yuan, M. Jiang, L. Yan, Y. J. Ding, *Appl. Catal., B*, **2021**, 293, 120208–120218.

[3] M. Xia, L. Qiu, Y. P. Li, T. Y. Shen, Z. Y. Sui, L.J. Feng, Q Chen, *Mater. Lett.*, **2022**, 307, 131078–131012.

[4] A. Phan, A. U. Czaja, F. Gandara, C. B. Knobler, O. M. Yaghi, *Inorg. Chem.*, **2011**, 50, 7388–7390.

[5] B. Wu, T. J. Lin, Z. X. Lu, X. Yu, M. Huang, R. O. Yang, C. Q. Wang, C. Tian, J. Li, Y. H. Sun, L. S. Zhong, *Chem*, **2022**, 8, 1658–1672.

[6] J. Liu, Y. Wei, R. T. Li, Y. X. Liu, H. L. Yu, X. Zhou, B. Wu, T. J. Lin, L. S. Zhong, *Appl. Catal., B*, **2024**, 350, 123951–123960.

[7] G. D. Qi, T. E. Davies, A. Nasrallah, M. A. Sainna, A. G. R. Howe, R. J. Lewis, M. Quesne, C. R. A. Catlow, D. J. Willock, Q. He, D. Bethell, M. J. Howard, B. A. Murrer, B. Harrison, C. J. Kiely, X. L. Zhao, F. Deng, J. Xu, G. J. Hutchings, *Nat. Catal.*, **2022**, 5, 45–54.